

Lithology, Pore-Filling Media, and Pore Closure Depth Beneath InSight on Mars Inferred From Shear Wave Velocities

Richard Kilburn¹ , Jharden Dasent¹ , Vashan Wright¹ , and Michael Manga² 

¹Scripps Institution of Oceanography, University of California San Diego, La Jolla, CA, USA, ²Department of Earth and Planetary Science, University of California Berkeley, Berkeley, CA, USA

Key Points:

- Mars' upper crust (0–8 km) beneath Interior Exploration using Seismic Investigations, Geodesy, and Heat Transport mission (InSight) comprises fractured gas-filled rocks and weakly cemented sediments
- Mars' deeper crust (8–20 km) beneath InSight could comprise fractured basalts or more-felsic igneous rocks with 0%–23% porosity
- No seismically detectable cryosphere exists in the crust and pores in the deeper crust host gas, liquid water, or up to 2% cement

Supporting Information:

Supporting Information may be found in the online version of this article.

Correspondence to:

R. Kilburn,
rkilburn@ucsd.edu

Citation:

Kilburn, R., Dasent, J., Wright, V., & Manga, M. (2022). Lithology, pore-filling media, and pore closure depth beneath InSight on Mars inferred from shear wave velocities. *Journal of Geophysical Research: Planets*, 127, e2022JE007539. <https://doi.org/10.1029/2022JE007539>

Received 24 AUG 2022

Accepted 17 NOV 2022

Author Contributions:

Conceptualization: Vashan Wright, Michael Manga
Data curation: Richard Kilburn, Jharden Dasent
Formal analysis: Richard Kilburn, Jharden Dasent, Vashan Wright, Michael Manga
Funding acquisition: Vashan Wright, Michael Manga
Investigation: Richard Kilburn, Jharden Dasent, Vashan Wright, Michael Manga
Methodology: Richard Kilburn, Jharden Dasent, Vashan Wright, Michael Manga
Project Administration: Vashan Wright, Michael Manga
Resources: Richard Kilburn, Vashan Wright, Michael Manga

Abstract We quantify the volume and distribution of water, cement, sediments, and fractured rocks within the Martian crust beneath NASA's InSight (Interior Exploration using Seismic Investigations, Geodesy, and Heat Transport mission) lander by using rock physics models to interpret shear wave velocities (V_s) measured from InSight data. The models assume that Mars' crust comprises sediments and fractured rocks whose pores and fractures host variable combinations of gas, liquid water, and mineral cements. Measured V_s in the upper crust (0–8 km) can be explained by layers of minimally (<2%) cemented sediments and gas-filled fractured basalts. Measured V_s in the deeper crust (8–20 km) can be explained by fractured basalts or more felsic igneous rocks (modeled here as 100% plagioclase feldspar) that is unfractured or has up to 23% porosity. Open pores in the deeper crust could host gas, liquid water, and up to 2% cement. Modeled V_s are too low for a seismically detectable ice-saturated cryosphere in the upper crust and temperatures are too high to freeze liquid water in the deeper crust. Notably, with V_s alone, we are unable to distinguish between liquid water and gas within the pores.

Plain Language Summary Liquid water may have existed on Mars as oceans, rivers, or ground water. Surface water was likely lost to space, buried as liquid water and ice, and/or incorporated in subsurface minerals and mineral cements. The InSight lander on Mars has a seismometer whose measurements can be used to estimate the velocity of seismic shear waves. Seismic velocities change based on rock type and the material that fills the pores within rocks (e.g., liquid water, gas, or ice and other mineral cements). We show that the measured seismic velocities in the upper (0–8 km) crust can be explained by layers of gas-filled basalts and minimally (2%) cemented sediments rather than ice-filled sediment or basalt. Measured seismic velocities in a deeper (8–20 km) crust can be explained by fractured basalt. More feldspar-rich rocks could explain the velocities in the deeper crust and they could be unfractured or have up to 23% porosity. Fractures within the deeper crust could host liquid water, gas, and up to a couple percent of mineral cements.

1. Introduction

Quantifying the volume and distribution of Mars' subsurface lithologies, mineral cements, and liquid water are critical to unraveling the planet's geologic evolution (Carr & Head, 2003, 2019; Di Achille & Hynes, 2010; Scheller et al., 2021). Mars' crust comprises igneous and sedimentary rocks that are lithified and fractured to varying degrees (Golombek et al., 2018; Pan et al., 2020; Tanaka et al., 2014). Two open questions are (a) what is the depth where pores close entirely within the Martian crust and (b) what percentage of existing pores in the Martian crust host liquid water or ice, or water incorporated into mineral cements.

Gravity and heat flow models provide constraints on Mars' subsurface porosity and pore closure depth (Goossens et al., 2017; Gyalay et al., 2020; Clifford, 1993; Clifford et al., 2010; Wieczorek et al., 2022). Constraining pore closure depth and how porosity changes with depth may help to constrain the pore-filling material of the crust, the crust water-carrying capacity, the maximum potential depth of aquifers (Gyalay et al., 2020; Clifford et al., 2010; Clifford, 1993), crustal densities and how to interpret seismic discontinuities (Wieczorek et al., 2022), and the geological and impact history of the Martian surface (Gyalay et al., 2020). Goossens et al. (2017) used gravity data to infer that Mars' average bulk density in the upper 20 km is $2,582 \pm 209 \text{ kg/m}^3$. From this bulk density, a porosity of 0.10–0.23 in the upper 20 km can be obtained. Wiecezorek et al. (2022) later integrated gravity and shear wave velocity data to hypothesize that a lower density (higher porosity) layer extends to 8 ± 2 or 20 ± 5 km below the surface and the pores close entirely beneath one of these depths. Knappmeyer-Endrun et al. (2021) used seismic inversions from receiver function analyses (via two different methods that used three marsquakes) to propose that the first two, km-scale, detectable seismic layers extend to 6–11 and 20 ± 5 km (Figure 1). Gyalay

Software: Richard Kilburn, Jhardel Dasent
Supervision: Vashan Wright, Michael Manga
Validation: Richard Kilburn, Jhardel Dasent, Vashan Wright, Michael Manga
Visualization: Richard Kilburn, Jhardel Dasent
Writing – original draft: Richard Kilburn, Jhardel Dasent
Writing – review & editing: Richard Kilburn, Jhardel Dasent, Vashan Wright, Michael Manga

et al. (2020) used heat flow models to argue that pore collapse via thermally activated viscous creep should occur between 12 and 23 km below the surface. The transition from open to closed pores should occur over 1 km (Gyalay et al., 2020). Gyalay et al. (2020) and Wieczorek et al. (2022) proposed pore closure depths between 8 ± 2 and 20 ± 5 km depth, making it unclear whether thermally activated viscous creep leads to pore closure at the base of the first seismic discontinuity or the top of the second seismic discontinuity (Figure 1).

Surface exposures alongside heat and fluid flow models provide constraints on the presence, volume, and distribution of water within the Martian crust. Rover and satellite images showing sediment structures and stratigraphy characteristic of ancient delta, marine, and fluvial depositional environments alongside direct and remotely inferred observations of ice and liquid water at the polar regions evidence past and current water on Mars (Baker, 2006; Carr, 1987; Nazari-Sharabian et al., 2020; Orosei et al., 2018). Evidence for past subsurface liquid water also includes Hesperian and Amazonian-aged outflow channels, whose discharges were sometimes a few orders of magnitude greater than Earth's largest floods (Bibring et al., 2005; Burr et al., 2002; Carr & Head, 2002; Colaprete & Jakosky, 1998; Di Achille & Hynes, 2010; Manga, 2004; Rodriguez et al., 2015; Voigt & Hamilton, 2018; Weiss & Head, 2017; Clifford et al., 2010). Mars' past surface water in rivers, lakes, and possible oceans may have been lost to space or infiltrated the ground (Bibring et al., 2005; Colaprete & Jakosky, 1998; Di Achille & Hynes, 2010). Liquid water may have percolated through the pores of rock whose permeability is higher (compared to Earth) due to Mars' lower gravitational acceleration and/or because impacts have created new fracture networks or increased hydraulic connectivity between existing networks (Clifford, 1997; Wang et al., 2005). Heat flow models suggest that a 0–9 and 10–22 km thick regional cryosphere could exist at Mars' equator and poles, respectively (Clifford et al., 2010). Atmospheric carbon dioxide may have dissolved in water, then precipitated as carbonate cement (up to 2%) (Adam et al., 2013; Boynton et al., 2009; Halevy & Schrag, 2009). Thus, mapping Mars' subsurface ice and other mineral cements, liquid water, and lithology may help constrain (a) the volume of water buried versus lost to space (Jakosky, 2021), (b) the planet's water budget and cycle through time (Clifford & Parker, 2001), (c) the fates of past surface water (Citron et al., 2018), (d) the volume of water sequestered by minerals, and (e) the lithology of Martian subsurface layers in the past and present (Mustard, 2019; Scheller et al., 2021; Wernicke & Jakosky, 2021).

Rock physics models and shear wave velocities V_s derived from seismograms collected by the seismometer (the Seismic Experiment for Interior Structure, SEIS) on the InSight (Interior Exploration using Seismic Investigations, Geodesy, and Heat Transport mission) lander provide opportunities to explore Mars' subsurface mechanical properties further. SEIS includes a 3-axis Very Broad Band seismometer and a 3-axis Short Period seismometer (Lognonné et al., 2019). SEIS is attached to the InSight lander and records ground motions (0.01–50 Hz) produced by a variety of sources, including marsquakes and meteorite impacts. V_s is sensitive to several rock and sediment properties, including mineralogy, fracture density, porosity, and ice and other mineral cements (Dvorkin & Nur, 1996; Jenkins et al., 2005; Mindlin, 1949; Waite et al., 2009). The Martian crust beneath InSight has at least two seismically detectable km-scale layers (Knapmeyer-Endrun et al., 2021). V_s are 1.7–2.1 km/s in the upper crust (i.e., between 0 and ~6–11 km) and 2–3.4 km/s in the deeper crust (i.e., between ~6–11 and 20 ± 5 km) (Figure 1). Interpretations using self-consistent fractured-media rock physics models (Berryman, 1980; Te Wu, 1966) indicate that V_s within the upper 6–11 km is lower than expected for a cryosphere (Manga & Wright, 2021; Wright et al., 2022). V_s between 6–11 and 20 ± 5 km may be consistent with basalts whose fractures are 1%–5% filled with calcite cement (Manga & Wright, 2021). Thus, Mars' subsurface is likely a mix of sediments (i.e., layers with unconsolidated grains) and fractured layers of consolidated sediments or igneous rocks.

Our study uses granular and self-consistent fractured-media rock physics models to infer the volume and distribution of liquid water, ice and other mineral cements, and lithology from InSight-measured V_s . Here, we focus on the composition of the crust down to the second seismic discontinuity, at 20 ± 5 km depth. Goossens et al. (2017); Knapmeyer-Endrun et al. (2021) propose both a 2- and 3-layer crust beneath InSight, indicative of the Moho depth at ~20 to 25 km (for a 2-layer crust) or ~39 to 47 km (for a 3-layer crust). Although we do not provide constraints on the Moho depth, we have focused on the second seismic discontinuity as both the thinner and thicker crustal density models support a seismic discontinuity at 20 ± 5 km below the surface. Our study builds upon previous studies (Heap, 2019; Li et al., 2022; Manga & Wright, 2021; Wright et al., 2022) by considering models for both fractured and granular media (Heap, 2019; Manga & Wright, 2021), using more recently constrained InSight-derived velocities (Manga & Wright, 2021), and/or interpreting seismic velocities constrained for a wider range of depths (0–20 km vs. the upper 300 m or 8 ± 2 km) (Li et al., 2022; Wright

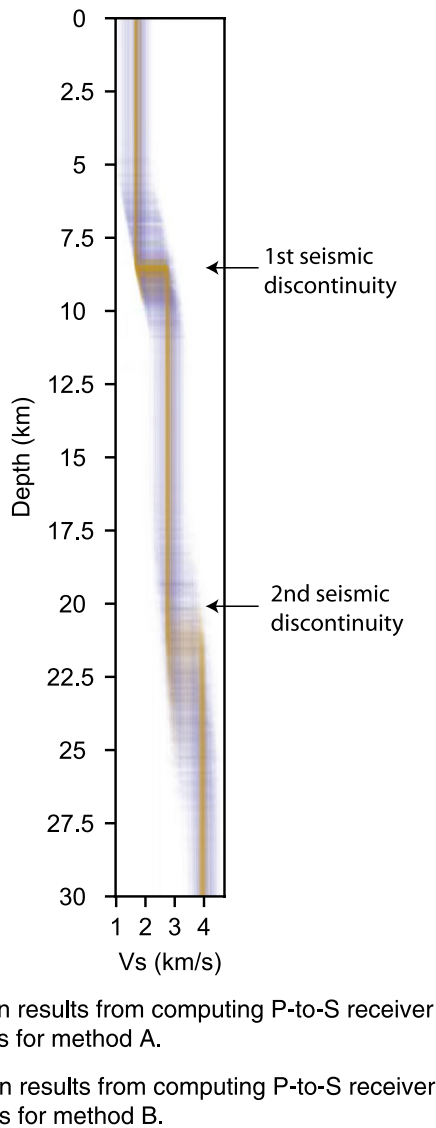


Figure 1. Interior Exploration using Seismic Investigations, Geodesy, and Heat Transport mission derived shear-wave velocities (V_s) (Knapmeyer-Endrun et al., 2021). The brown and purple lines show V_s from results obtained from two different approaches for conducting P-to-S receiver function inversions for travel-time data whose source were from three marsquakes. The first seismic discontinuity is at 6–11 km. Knapmeyer-Endrun et al. (2021) interpreted this discontinuity as the bottom of the upper crust. The second seismic discontinuity is at 20 ± 5 km and Knapmeyer-Endrun et al. (2021) interpreted this discontinuity as the bottom of the deeper crust.

elastic micro-scale slip during seismic wave propagation and rough grain contacts do not), porosity ϕ , effective stress P , and coordination number c_n (average number of grains contacting each other). In order to use the granular media models, we calculate mineral Poisson's ratio ν_m using

$$\nu_m = \frac{3\kappa_m - 2\mu_m}{6\kappa_m + 2\mu_m}, \quad (3)$$

where μ_m and κ_m are mineral shear and bulk moduli. We calculate mineral Poisson's ratio ν_m using Equation 3 from the granular media models as the Poisson's ratio for the constituents with the elastic moduli we used were unavail-

et al., 2022). Here, we infer that (a) the upper crust beneath InSight comprises layers of fractured gas-filled basalts and weakly cemented sediments, (b) the deeper crust could be fractured basalts or more felsic igneous rocks that are either unfractured or has up to 23% porosity, (c) the pores of fractured rocks in the deeper crust could host liquid water, gas, or 2% cement and 98% liquid water or gas, and (d) no seismically detected ice-saturated cryosphere layer exists beneath InSight.

2. Methods

We compare modeled and measured V_s to infer Mars' subsurface mechanical properties, constraining model uncertainties with Monte Carlo simulations and sensitivity analyses. We use granular and fractured-media rock physics models to model V_s in the upper crust; we use only the fractured-media models for the deeper crust because we do not expect sediment layers in the deeper crust.

We calculate V_s from

$$V_s = \sqrt{\frac{\mu_e}{\rho}}, \quad (1)$$

where μ_e and ρ are the effective shear modulus and bulk density, respectively. Rock physics models, described next, provide estimates for μ_e (see Supporting Information S1 for equations). We estimate bulk density ρ using

$$\rho = \sum_i \phi_i \rho_i, \quad (2)$$

where ρ_i and ϕ_i are the mineral/fluid densities and volume fractions of the i th constituents, respectively, which, when combined may be used to estimate bulk density ρ (Equation 2).

2.1. Modeling V_s for Sediments

We estimate μ_e for cementless sediments using the Hertz-Mindlin rock physics model (Mindlin, 1949). The cementation model (Dvorkin & Nur, 1996) provides μ_e for sediments with cements (e.g., ice and calcite) deposited at grain contacts or that surround grains in contact. We modeled calcite because calcite may have precipitated from carbon dioxide-rich groundwater, calcite is a common cementing mineral on Earth, and Ming et al. (2009) suggested calcite as a likely cementing material on Mars based on data obtained during the Phoenix Mission. The models' equations can be found in Method S1 in Supporting Information S1, Mindlin (1949), Dvorkin and Nur (1996), and Mavko et al. (2020). Model input parameters are mineral Poisson's ratio ν_m , mineral bulk moduli κ_m , mineral shear moduli μ_m , cement fraction c_p , volume fraction of rough versus smooth grain contacts f (smooth grain contacts allow

Table 1
Mineral Shear (μ_m) and Bulk (κ_m) Moduli, and Mineral Density (ρ) Used in This Study

Mineral	μ_m (GPa)	κ_m (GPa)	ρ (kg/m ³)	References
Calcite	28.2	71.6	2,710	Mavko et al. (2020)
Basalt	40.0	80.0	2,900	Christensen (1972) and Heap (2019)
Clay	6.0	12.0	2,650	Vanorio et al. (2003)
Halite	15.3	25.2	2,160	Zong et al. (2017)
Ice	3.8	8.7	1,220	Toksöz et al. (1976)
Plagioclase	25.6	75.6	2,630	Woeber et al. (1963)

able. Representative minerals within Mars' subsurface and their respective μ_m and κ_m are in Table 1. We treat basalt and clay as single mineral constituents. We estimate porosity ϕ changes with depth using

$$\phi = \phi_0 e^{-\frac{z}{k}}, \quad (4)$$

where z , k , and ϕ_0 are depth in km, a porosity reduction constant scaled for Mars' gravitational field, and ϕ at the surface, respectively. Clifford (1987) estimated $k = 2.82$ km based on scaling lunar observations; we consider values that range from 1 to 10 km. We assume that ϕ_0 is between 0.3 and 0.5, consistent with studies that constrained ϕ_0 from rover measurements and analog Earth studies (Golombek et al., 2018; Lewis et al., 2019; Lognonné et al., 2020; Smrekar et al., 2019). Effective stress P is

$$P = \rho g h - P_f, \quad (5)$$

where g , h , and P_f are gravitational acceleration on Mars (3.71 m/s²), depth, and fluid pressures, respectively. Coordination number c_n is from Mavko et al. (2020)

$$c_n = 20 - 34\phi + 14\phi^2. \quad (6)$$

We use the input parameters described above to calculate μ_e from the rock physics model equations, then V_s from Equation 1.

To compare measured and modeled V_s , we create a rock physics template that relates V_s to ϕ (0–0.5), grain-contact friction (100% rough or smooth grain contacts), and pore ice percentage (0%–100%) for ice deposited at grain contacts or surrounding grains in contact. Then, we identify the combinations of ϕ , grain contact friction, and/or pore ice percentage that are consistent with the measured V_s . We also compare measured and modeled V_s directly; these models assume a porosity reduction profile (Equation 4) and that pores host either 99% ice and 1% gas, 100% gas, 100% liquid water, 2% calcite cement and 98% gas, or 2% calcite cement and 98% liquid water. We model a cryosphere as 99% ice and 1% gas because the cementation model breaks down for the 100% ice limit, where 0% porosity introduces indeterminacy into the equations. We use a 10,000 realization Monte Carlo simulation to incorporate input parameter uncertainties into the results from the models used for direct comparisons with measured V_s . During the Monte Carlo simulation, we randomly select a new ϕ -depth profile for each realization. Selected ϕ values influence coordination number, bulk density, and effective stress.

2.2. Modeling V_s for Fractured Rocks

We estimate μ_e for fractured rocks using the self-consistent model of Berryman (1980). The model's equations can be found in Method S1 in Supporting Information S1, Berryman (1980), and Mavko et al. (2020). The model's input parameters are μ_m , κ_m , ϕ , and pore shape (defined by the aspect ratio, α —i.e., the pore's short axis divided by the long axis). We calculate μ_e assuming that the fractures within a basalt contains either 100% gas, 100% water, 98% gas and 2% calcite cement, 98% water and 2% calcite cement, and 10%–100% ice. We then use μ_e and ρ to calculate V_s from Equation 1. We use these results to create rock physics templates relating V_s to ϕ (0.1–0.5), α (0.03–1) to account for a wide range of inclusion shapes (as the differences in modeled seismic velocities assuming α less than 0.03 are not significant and would not change our interpretations), and pore ice, water, gas, and cement percentages. Last, we identify the ranges of ϕ , α , and pore-filling media that best explain measured V_s . In selecting our aspect ratio ranges, we followed the examples from previous studies that considered aspect ratios of 0.03–1 (Heap, 2019), 0.03–1 (Manga & Wright, 2021; Wright et al., 2022), and 0.01 (Li et al., 2022). While both our study and Heap (2019) use fractured media models, Heap (2019) used the Kuster Toksöz (KT) fractured media model that approximates the elastic moduli through a first-order, long-wavelength scattering theory. The Berryman fractured media model uses the “self consistent” approximation. The KT model does not allow the inclusions (cracks) to overlap, while the Berryman model does. The Berryman model also allows for a higher concentration of inclusions.

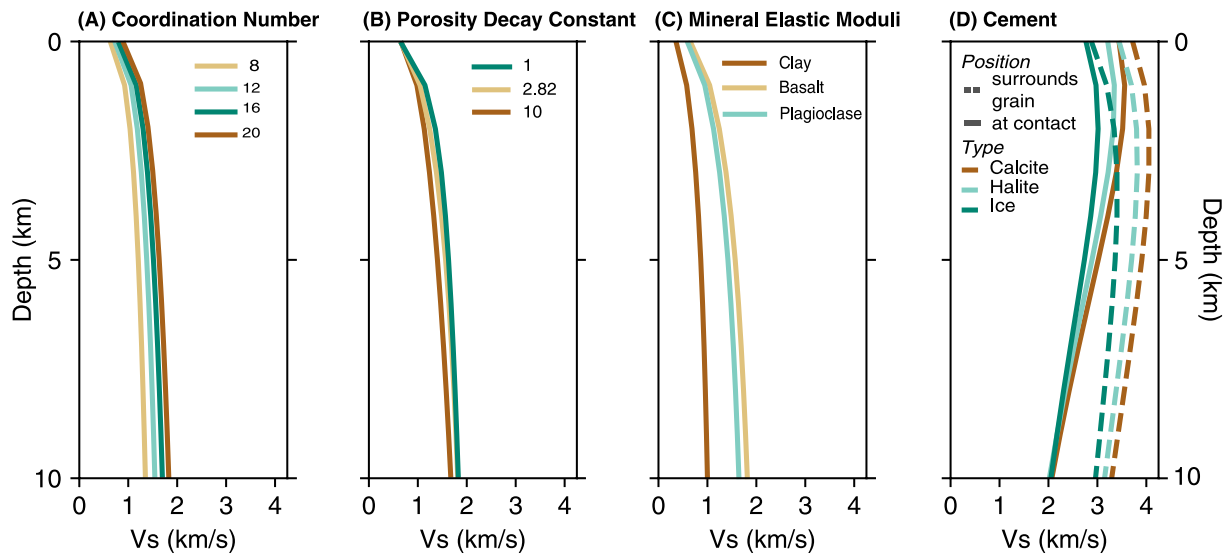


Figure 2. Effects of (a) coordination number, (b) porosity decay constant (km), (c) mineral moduli, and (d) cement type and location on V_s . We first assume that the subsurface comprises 100% basalt, porosity reduce exponentially with depth from $\phi_0 = 0.4$, c_n is primarily controlled empirically by ϕ as shown in Mavko et al. (2020), and no mineral cements exist between grains and pores. Then, we only change the parameters being assessed in each graph to assess their influence on V_s .

2.3. Sensitivity Analyses

We conduct sensitivity analyses to assess how model parameter uncertainties could influence interpretations as well as to identify which rock properties are resolvable with our models. We first assume that gas fills the pores and there is no cement within the pores. Then we vary a single input parameter to assess how its uncertainty influences modeled V_s . For granular media models, we assume that ϕ_0 is 0.4 and exponentially decays with depth. We vary mineralogy (100% basalt, plagioclase feldspar, or clay), coordination number (8, 12, 16, or 20), porosity decay constant (1, 2.82, or 10 km), cement type (98% gas and 2% calcite, halite, or ice), and cement location (at grain contacts or entirely surrounds grains). For fractured media models, we set α from 0.01 to 1 and vary host rock composition (100% plagioclase feldspar or clay) then find the V_s difference between the compositionally varied and a basalt host rock.

3. Results

3.1. Sediments

The ability to resolve changes in subsurface properties of sediment layers is most affected by uncertainties in cement type and location, followed by μ_m and κ_m , c_n , and ϕ (Figure 2). Assuming 100% basalt or plagioclase feldspar grains as representative of the compositional diversity of igneous rocks (and all else equal) results in a V_s difference of ~ 0.20 km/s (Figure 2c), which is within the measured V_s uncertainties (Figure 1). Thus, it is challenging to use the granular media rock physics models alone to distinguish between plausible igneous compositions. Clay layers may be seismically distinguishable from igneous rock layers since the differences in their V_s predictions are 0.95 and 0.72 km/s, respectively. Uncertainties in the porosity decay constant k (i.e., 1, 2.82, and 10) produce a V_s range of ~ 0.28 km/s (Figure 2b); this result implies that the assumed decay constant does not significantly influence the interpretations of measured V_s . The range for the modeled V_s difference for coordination numbers of 8, 12, 16, and 20 is 0.56 km/s, which is within the uncertainty of measured V_s (Figure 2a). Assuming 2% calcite, ice, and halite mineral cement produce V_s ranges of ~ 1.18 and ~ 0.64 km/s for the cement at grain contacts versus on the grain surface, respectively (Figure 2d). Assuming calcite and ice cement at grain surfaces predicts comparable velocities at all depths (i.e., within ~ 0.05 km/s), implying that we can not distinguish between a few (<2) percent pore ice and calcite cement based on V_s alone.

Figure 3 shows the granular media rock physics template relating V_s , porosity, pore-filling media, and grain contact friction for modeled sediment layers. Measured V_s are consistent with modeled V_s for sediments comprised of 100% rough-grain contacts and sediments that host a few percent ice in their pores (Figure 3). Models for

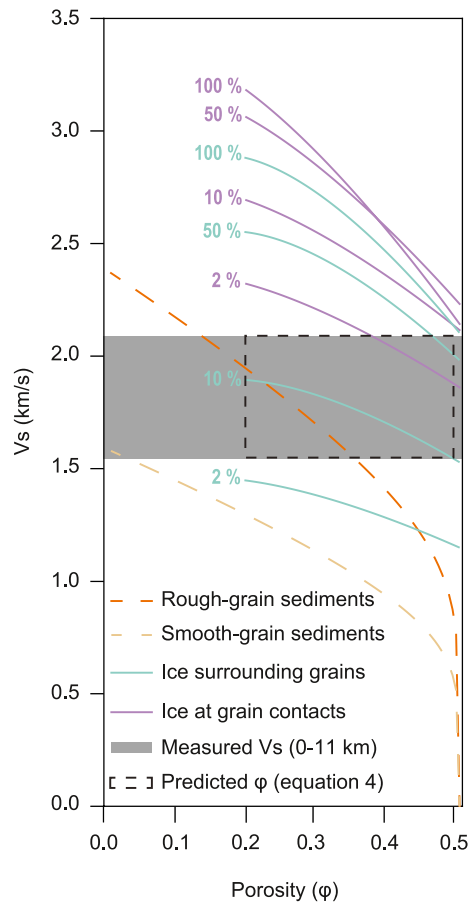


Figure 3. Rock physics template relating V_s , porosity, pore ice percentage, and sediments composed of 100% rough or smooth grain contacts. Calculations are based on the Hertz Mindlin and Cementation granular media models.

sediment with 100% rough-grain contacts are consistent with measured V_s if the sediments' porosities are between 0.14 and 0.35. Models with 100% smooth grain contacts underpredict measured V_s for all porosities between 0 and 0.5. Models for sediments that host 10%–18% ice that surrounds grains in contact are consistent with the measured V_s if porosities are between 0.2 and 0.5. If pores are filled with 2% ice deposited at grain contacts, the porosities need to be 0.4–0.5 to explain the measured V_s . The measured V_s are consistent with modeled V_s for sediments with ice deposited at grain contacts if the pore-ice percentage is less than 2% and porosities are higher than 0.37.

Assuming a porosity-depth reduction relationship defined by Equation 4, where $k = 2.82$ km, provides additional insights into the volume and type of pore-filling materials that could explain measured V_s within the upper crust. Measured V_s are most consistent with modeled V_s for a sediment with basalt grains and whose pores are filled with gas or 2% calcite cement (Figures 4b and 4d). In general, Hertz-Mindlin rough-grained models predict V_s with lower misfits than the smooth-grained models. The smooth-grained model underpredicts V_s by 0.53 km/s for a gas-filled sediment layer in the upper crust (Figure 4b). The liquid water saturated smooth-grained model underpredicts V_s by 0.61 km/s in the upper crust (Figure 4c). The rough-grained models for a gas or liquid water-filled layer predicts higher V_s than the smooth-grained models in the upper crust by 0.4 km/s. Assuming that calcite cement fills 2% of the pores and liquid water or gas fills the remaining 98% predict V_s within $\pm \sim 0.42$ km/s of measured V_s , regardless of whether the cement is deposited at grain contacts or surrounds grains (Figures 4d and 4e). Assuming ice-saturated pores overpredicts measured V_s by 1.6 km/s (Figure 4a).

3.2. Fractured Rocks

V_s of fractured rocks are most sensitive to α , ϕ , and elastic moduli of the host rock (Figures 5–7). As expected, V_s increases as porosity decreases and α increases. The difference in V_s between basalt and other host rocks (e.g., plagioclase feldspar and clay) increases with decreasing porosity and increasing aspect ratio. A plagioclase host rock produces a difference of 0–0.5 km/s in V_s

compared to a basalt host rock, for all pore-filling media (Figure 6). Thus, we can only distinguish between basalt and plagioclase rocks with V_s differences >0.3 km/s. A clay versus basalt host rock lowers V_s by ~ 0.4 –2 km/s for gas, ~ 0.15 to 2 km/s for liquid water, ~ 0.2 to 2 km/s for 2% calcite cement and 98% gas, and ~ 0.3 to 2 km/s for 2% calcite cement and 98% liquid water (Figure 7). Figure 7 shows the combinations of aspect ratio and porosities for when a clay and basalt host rock is resolvable (i.e., contour lines with V_s of at least 1.2 km/s).

A basalt host rock whose fractures are filled with varying percentages of ice, gas, water, and or calcite cement could explain the measured V_s in the upper and deeper crust. The upper crust could be filled with 100% gas, 100% liquid water, or 2% calcite cement with 98% gas or liquid water (Figure 5). Of these, a 100% gas-filled basalt (Figure 5a) produces the smallest number of ϕ – α combinations ($\phi = 0.1$ –0.47 and $\alpha = 0.03$ –1) that could explain the measured V_s . A 2% calcite cemented basalt (Figures 5c and 5d) produces the largest combinations of ϕ – α that could explain the measured V_s . Modeled V_s for basalts with ice that fills 20%–60% of the pores are consistent with measured V_s if ϕ is between 0.2 and 0.5. The measured V_s in the deeper crust are consistent with modeled V_s for a basalt filled with 100% gas or liquid water, 2% calcite cement with 98% gas or liquid water, or 10%–100% ice (Figure 5, Figure S1 in Supporting Information S1). A 100% gas-filled basalt (Figure 5a) produces the smallest number of ϕ – α combinations ($\phi = 0.1$ –0.4 and $\alpha = 0.04$ –1.0) that could explain the measured V_s , while 60% ice-filled basalt host rock produces the largest number of ϕ – α combinations ($\phi = 0.1$ –0.5 and $\alpha = 0.03$ –1.0) (Figure 5i).

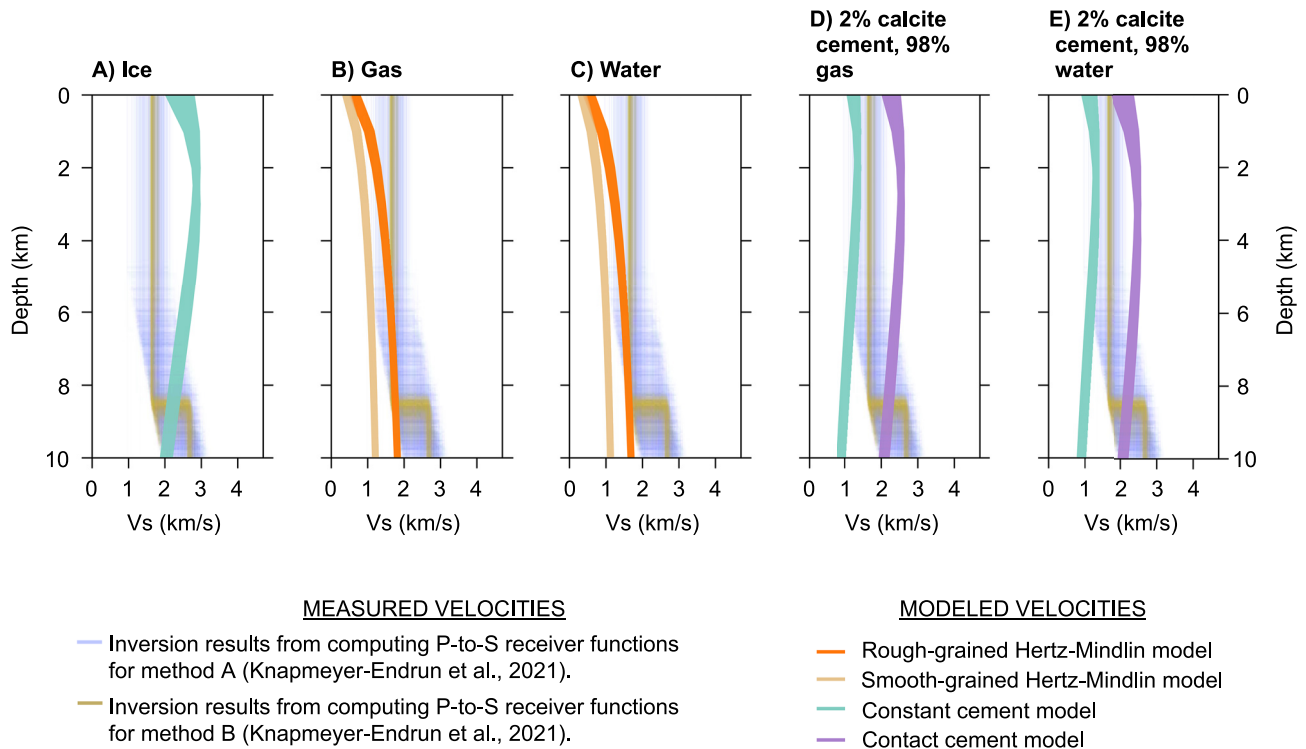


Figure 4. Comparisons of modeled and predicted V_s assuming basalt grains with pores filled with: (a) 99% ice and 1% gas, (b) 100% gas, (c) 100% water, (d) 2% calcite cement and 98% gas, and (e) 2% calcite cement and 98% water. Calculations are based on the Hertz Mindlin and Cementation granular media models.

4. Discussion

Our interpretations are guided by limitations associated with rock physics model assumptions, uncertainties in model parameters and measured V_s , available satellite and rover images, gravity-derived bulk density data, and heat flow models. The rock physics models provide end-member V_s estimates for the hypothesized stratigraphy (i.e., either sediments or fractured rocks filled with varying percentages of gas, liquid water, or ice and other mineral cements). Martian subsurface stratigraphy may include a mixture of fractured igneous rocks (e.g., basalts or 100% plagioclase feldspar) emplaced as volcanic lava flows or intrusions with varying physical (e.g., porosity) and mechanical (e.g., elastic properties) properties (Heap & Violay, 2021), brecciated sedimentary rocks, sands, and clays (Golombek et al., 2018; Pan et al., 2020; Tanaka et al., 2014; Warner et al., 2022). Thus, the measured V_s could be averages from several smaller rock and sediment layers that are not resolvable by the seismic velocity models (Knapmeyer-Endrun et al., 2021). Considering these limitations, our primary interpretations are that the upper crust comprises fractured basalt and cemented sediment layers whereas the deeper crust could comprises gas or water-filled fractured basalt with open, partially cemented fractures or more felsic igneous rock (represented here by 100% plagioclase feldspar) layers with 0%–23% porosity.

4.1. Fractured Rocks and Cemented Sediments Within the Upper Crust

Our comparisons of measured and modeled V_s suggest that gas-filled fractured rock and cemented sediment layers may coexist within the upper crust. We interpret that the upper crust is gas-filled because temperatures in the upper crust would freeze water (Clifford et al., 2010). Sediments filled with 2% cement and 98% gas and basalts filled with gas are possible within the upper crust since their modeled V_s are consistent with measured V_s when we parameterize the models with the gravity-derived porosity range (0.10–0.23) (Figure 4; Goossens et al., 2017). The coexistence of the gas-filled basalt and weakly cemented sediment layers would be resolved as one seismic velocity layer in seismic velocity models since differences in the layers' V_s would not produce a large impedance contrast. Additional support for the potential coexistence of igneous rock and sediment layers in the upper crust comes from (a) Martian meteorites and images of surface-exposed stratigraphic columns that evidence basalts, sandstones, and sediments in the upper 1 km of the crust (Carr & Head, 2002; Edwardset al.,

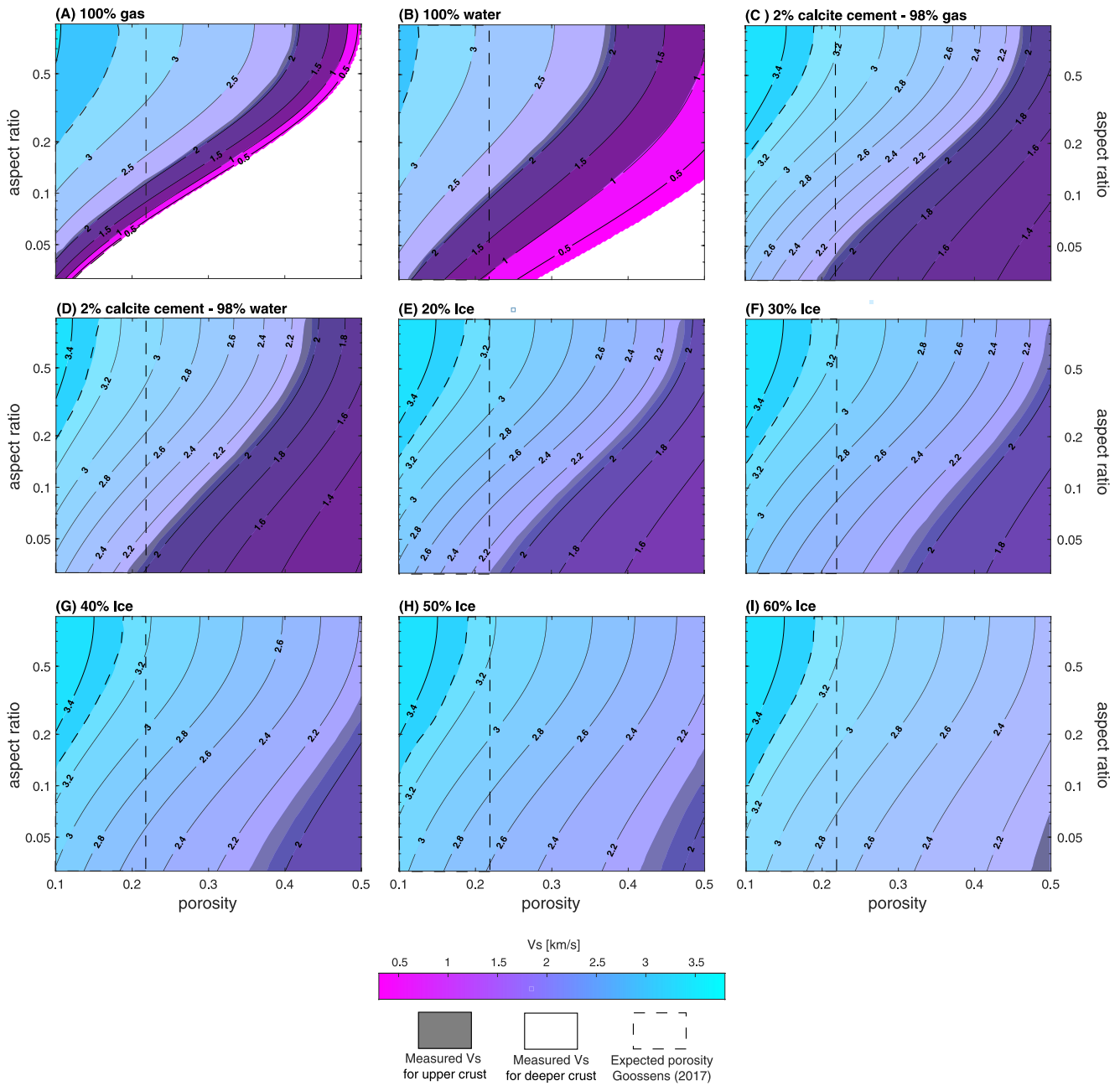


Figure 5. Rock physics template showing the V_s relationship between α (0.03–1.00), ϕ (0.1–0.5), varying pore-filling media, and varying pore-filling ice percentage. The black shading shows V_s for the upper crust; the white shading shows V_s for the deeper crust. The pore spaces are filled with either (a) gas, (b) water, (c) 2% calcite cement and 98% gas, (d) 2% calcite cement and 98% water, or (e) 20%, (f) 30%, (g) 40%, (h) 50%, or (i) 60% ice. Y-axis is logarithmic.

2011; McSween, 2015; Golombek et al., 2018; Hobiger et al., 2021; Knapmeyer-Endrun et al., 2021) and (b) InSight-derived high-resolution seismic velocities that are consistent with gas-filled basalt and sediment layers down to 0.3 km below the surface of the landing site (Hobiger et al., 2021; Wright et al., 2022). Other layers with different lithologies and pore-filling media, and hence different V_s , may exist within the upper crust. If so, these layers are likely too thin to be detected by the longer period marsquake waves used by Knapmeyer-Endrun et al. (2021) to constrain the V_s -depth structure. Seismic anisotropy may also provide constraints on fracture orientations (Li et al., 2022).

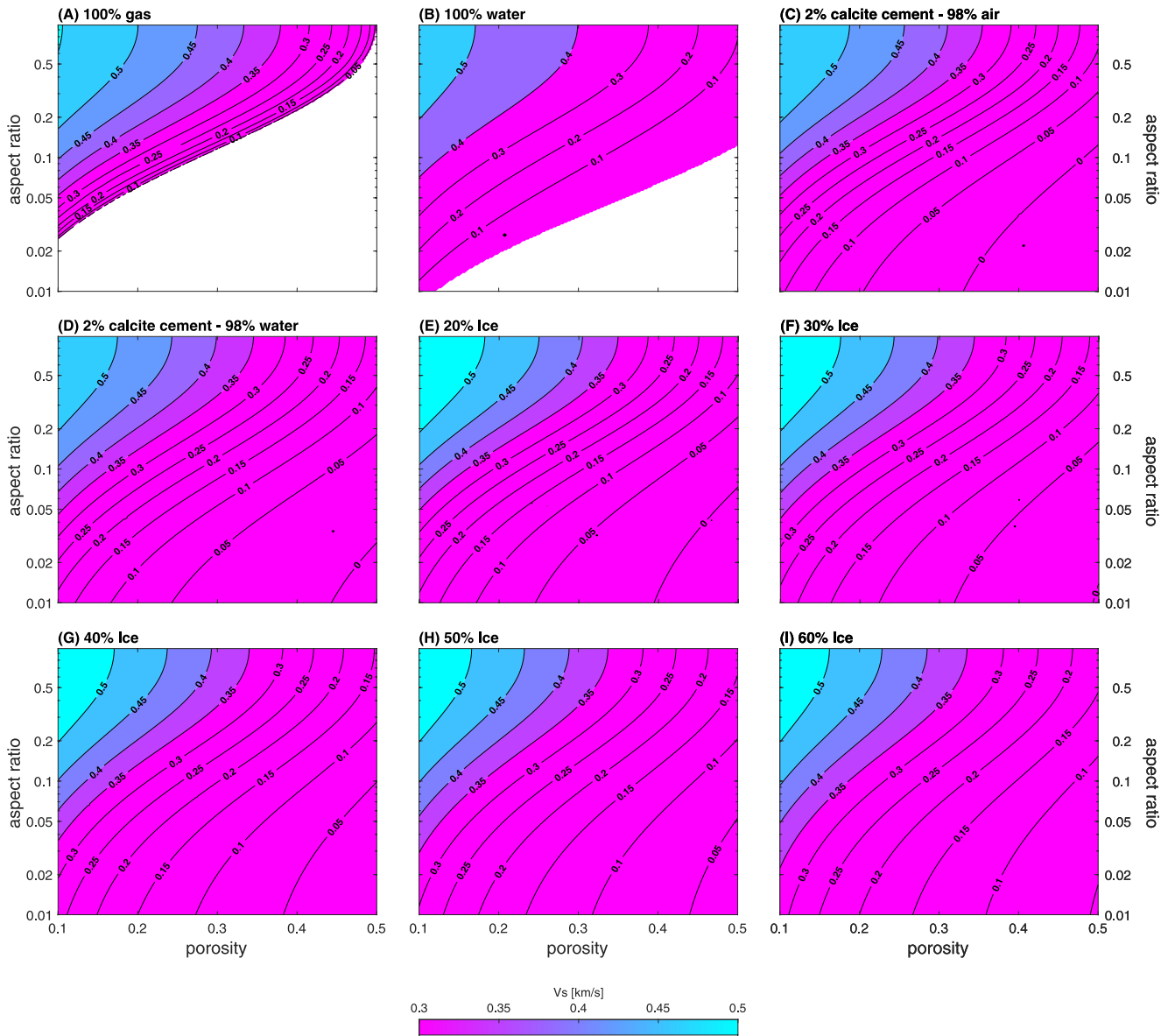


Figure 6. Rock physics sensitivity template showing the V_s difference between a basalt and plagioclase feldspar host rock. V_s changes with α (0.01–1.00), ϕ (0.1–1), and pore-filling media. The pores are filled with either (a) gas, (b) water, (c) 2% calcite cement and 98% gas, (d) 2% calcite cement and 98% water, or (e) 20%, (f) 30%, (g) 40%, (h) 50%, or (i) 60% ice. Y-axis is logarithmic.

4.2. No Ice-Saturated Cryosphere in the Upper Crust

There is likely no cryosphere within the upper crust, beneath InSight. The lack of a cryosphere is indicated by observations that when ice-filled, the granular media models overpredict measured V_s by 0.5–2 km/s (Figure 4a) and that, for fractured basalts, there are no modeled combinations of porosity and pore shape that would explain the measured V_s if we restrict porosity to 0.10–0.23, as estimated by Goossens et al. (2017) (Figures 5e–5i). One possibility not captured by our models is that there exists mushy ice (i.e., mix of soft, snow-like, ice and brine) within the pores of rocks and sediments deposited at depths greater than a few hundred meters, depending on regional heat flow. Detecting a mushy ice may require improved constraints on attenuation beneath InSight and developing models connecting seismic velocities, attenuation, and mushy ice concentrations (Dou et al., 2017). This can be done using lab and permafrost experiments.

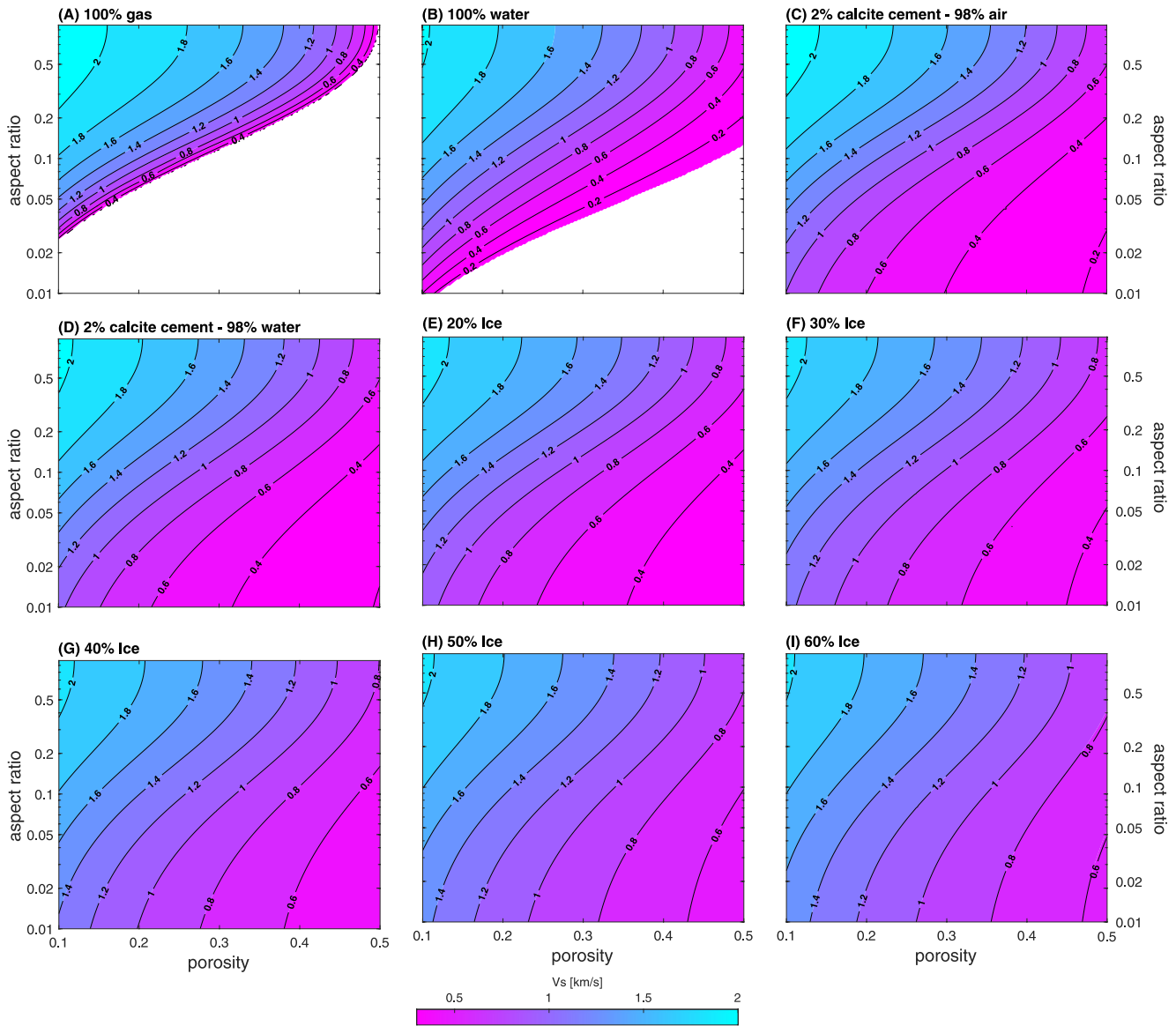


Figure 7. Rock physics sensitivity template showing the V_s difference between a basalt and clay host rock. V_s changes with α (0.01–1.00), ϕ (0.1–0.5), and pore-filling material. The pores are filled with either (a) gas, (b) water, (c) 2% calcite cement and 98% gas, (d) 2% calcite cement and 98% water, or (e) 20%, (f) 30%, (g) 40%, (h) 50%, or (i) 60% ice. Y-axis is logarithmic.

4.3. Mineralogy, Pore Collapse, and Pore-filling Media in the Deeper Crust

Our model comparisons, the reliability of fractured media models for predicting V_s of very low ϕ (<3%) basalts, and differences in the effective pressures and heat flow between Earth and Mars lead us to interpret that, if basaltic, the deeper crust has 10%–23% porosity. The measured V_s in Mars' deeper crust are 0.4–1.7 km/s lower than V_s for modeled unfractured basalts. Fractured media rock physics models successfully predict V_s of very low ϕ (<3%) basalts with as little as 0%–2% misfit (Tsuji & Iturrino, 2008). Our model predicts V_s of ~ 3.7 km/s for unfractured ($\phi = 0$) Martian basalts, assuming the mineral elastic moduli and densities listed in Table 1. If the deeper crust is basaltic and pores are filled with gas, liquid water, or 2% cement and 98% gas or liquid water, Mars' comparatively lower V_s may be explained by basalt layers with $\alpha = 0.15$ – 0.8 , $\phi = 0.10$ – 0.23 (Figures 1 and 5), and bulk density $\rho = 2,318$ – $2,713$ kg/m³ (Equation 2). These ρ and hence ϕ ranges are consistent with Goossens et al. (2017) gravity-derived bulk density and porosity ranges for the deeper crust. The porosity of Earth ocean basalts reduce by $\sim 90\%$ from 0 to 6 km depth (Chen et al., 2020). At 6 km below the surface of Mars, assuming $\phi = 0.10$ (the lower ϕ limit proposed by Goossens et al. (2017)) and gas or liquid water fills the host rock, Earth's

effective pressure is ~ 3 times greater than Mars' (Equation 5). Earth's average heat flux is ~ 4.8 times greater than Mars' average (Davies & Davies, 2010; Parro et al., 2017). Manning and Ingebritsen (1999) estimates that viscous creep-induced pore collapse occurs at an average depth of ~ 12 km on Earth. Thus, we infer that Mars' lower effective stress, heat flow, and gravitational acceleration would cause elastic pore closure to occur at depths deeper than 12 km. Our findings and interpretations imply that a basaltic host rock would require 10%–23% porosity and effective pressure-induced pore collapse may occur at the same depth as the second seismic discontinuity, located at the base of the deeper crust. This interpreted depth of pore collapse does not preclude the possibility that thermally activated pore collapse occurred in the deeper crust in the past (Gyalay et al., 2020), and currently open pores may have been created by subsequent surface impacts or other stresses.

Our model comparisons show that the V_s in the deeper crust is also consistent with a plagioclase feldspar host rock with 0%–23% porosity. Wicczorek et al. (2022) proposed that Mars' V_s may be lower than unfractured basalt's because the Martian crust comprises more felsic, feldspar-dominated igneous rocks whose density and shear moduli, and hence V_s , are lower than those of basalt. Payré et al. (2019) used visible and near infrared spectroscopy to identify excavated feldspar-rich crust, and based on thermal infrared data suggests that underneath a basaltic surface, the deeper crust has a more evolved feldspar-rich composition. We represent the felsic end-member igneous rock as a 100% plagioclase feldspar host rock. Our modeled V_s of an unfractured plagioclase host rock is ~ 3.1 km/s, which falls in the upper 75% quartile of the InSight-derived V_s range for the deeper crust (Figure 1) and supports the idea that the measured V_s on Mars could be explained by zero porosity (unfractured) plagioclase feldspar. We note that the two groups of InSight-derived measured V_s on Mars, based on P-S receiver function inversion from three marsquakes using two different methods, overlap at ~ 2.6 to 2.75 km/s (Figure 1). If the deeper crust comprises 100% plagioclase and it is fractured and filled with gas, liquid water, or 2% cement and 98% gas or liquid water, the measured V_s in the overlapping range may also be explained by layers of 100% plagioclase feldspar whose $\alpha = 0.07$ –0.97, $\phi = 0.10$ –0.23 (Figures 1 and 6, Figure S2 in Supporting Information S1), and bulk density $\rho = 2,277$ –2,601 kg/m³ (Equation 2). These ϕ and ρ ranges are consistent with Goossens et al. (2017) gravity-derived ϕ and ρ ranges for the deeper crust. If the host rock is 100% plagioclase and unfractured, viscous creep-induced pore closure may occur at the same depth as the shallower seismic discontinuity, located at the top of the deeper crust. If up to 23% porosity exists, the onset of viscous creep-induced pore closure may occur at the same depth of the deeper seismic discontinuity, located at the base of the deeper crust; the porosity may also be due to post-pore-closure impact fracturing or other stresses. The higher V_s of the Northern deeper lowlands crust, 3.2 km/s (Kim et al., 2022), may reflect a more mafic composition or a less fractured crust than that below InSight. Together, our analyses suggest that if the host rock is 100% plagioclase, the deeper crust is unfractured with pore closure occurring at the shallower seismic discontinuity or hosts up to 23% porosity, which is filled with gas, liquid water, or 2% cement and 98% gas or liquid water. In the latter scenario, pore closure occurs at the deeper seismic discontinuity. Alternatively, the basalts could have been significantly chemically and or hydrothermally altered due to heavy bombardment and impact cratering, or interactions with fluid flow and increased geothermal heat. Bolide impact and cratering processes still exist today and may continue to minimize the effect of viscous pore closure (Broglia & Ellis, 1990; Franzson et al., 2010; Heap et al., 2021).

If porosity exists, pores in the deeper crust could be filled with gas, liquid water, or 2% cement and 98% gas or liquid water. We can not distinguish between gas and water-filled pores in the deeper crust since the V_s difference between a gas- and water-filled host rock at this depth is less than 0.1 km/s (Figures 5a–5d, Figure S2 in Supporting Information S1) and the modeled geothermal gradient on Mars suggest that liquid water could be stable beneath 8 km (Clifford et al., 2010). Though the measured V_s are consistent with a fractured host rock whose pores are ice filled, we infer that ice does not fill the pores because temperatures in the deeper crust are too high to freeze water brine (Clifford et al., 2010). Pores are likely filled with at least 2% cement because models for a 2% calcite cemented crust with 98% gas or liquid water are consistent with measured V_s within the gravity-derived porosity range (0.10–0.23) (Goossens et al., 2017). Apart from calcite, other non-ice mineral cements could exist within the pores since the differences between the elastic mineral moduli of calcite and other expected cements within Mars' crust (Table 1) result in V_s differences no greater than ~ 0.1 km/s if cement fills 2% of the pores. Cements usually precipitate from liquid water solutions. If the source of liquid water in the deeper crust is from the surface or upper crust, this liquid water needed to percolate to the deeper crust before temperatures in the upper crust became cold enough to freeze liquid water. Modest amounts of deeper crustal liquid water could also be supplied by intrusive magma below or within the deeper crust (Black et al., 2022).

5. Conclusions

This study uses rock physics models and shear wave velocities V_s to constrain the volume and distribution of subsurface liquid water, mineral cements, and lithology beneath InSight on Mars. The upper crust (0–8 km) most likely comprises gas-filled fractured basalts and minimally cemented (up to 2% in pores) sediment layers. Measured V_s in the upper crust are too low for an ice-saturated cryosphere layer. The deeper crust (8–20 km) comprises consolidated basalts or more feldspar-rich rocks whose fractures have not closed entirely and may be filled with gas, water, or 2% non-ice mineral cements and 98% gas or liquid water. The range of measured V_s in the deeper crust are also consistent with unfractured feldspar. The presence and quantity of liquid water in the pores would be better resolved by integrating our results with constraints from compressional wave velocities.

The results of this study have implications for the thermal and hydrogeological history of the Martian subsurface beneath InSight. Pores within the deeper crust could remain open because the processes creating porosity (e.g., chemical reactions such as dissolution or impact cratering) are more dominant than thermally activated viscous creep-induced pore collapse. Pores could also be currently open because they were created by impacts after the rocks experienced pore collapse induced by viscous creep. Open pores could host liquid water that, if sourced from the surface or the upper crust, percolated to the deeper crust before temperatures became colder, freezing the water on its way down. Alternatively, liquid water could be introduced to the deeper crust via magmatic processes. These results could be significant to unlocking the subsurface thermal evolution of Mars, providing guidance on the search for life and water on Mars, and informing the potential for in-situ resource utilization if humans were to visit Mars.

Data Availability Statement

Codes used in this study can be found at Kilburn et al. (2022). The InSight-derived seismic velocities that we used in this study are available in Knapmeyer-Endrun et al. (2021).

Acknowledgments

R. Kilburn, J. Dasent, and V. Wright acknowledge support from the National Science Foundation Grant 2136301. M. Manga acknowledges support from the CIFAR Earth 4D program and the NASA Grant 80NSSC19K0545. The authors thank the NASA and the InSight team for their dedication, hard work, and vision, especially during this time when COVID-19 is real. The authors also thank the Mars, No Structure, Just Vibes retreat for providing a welcoming environment and support during the writing of this manuscript.

References

- Adam, L., van Wijk, K., Otheim, T., & Batzle, M. (2013). Changes in elastic wave velocity and rock microstructure due to basalt-CO₂-water reactions. *Journal of Geophysical Research: Solid Earth*, 118(8), 4039–4047. <https://doi.org/10.1002/jgrb.50302>
- Baker, V. R. (2006). Geomorphological evidence for water on Mars. *Elements*, 2(3), 139–143. <https://doi.org/10.2113/gselements.2.3.139>
- Berryman, J. G. (1980). Long-wavelength propagation in composite elastic media I. Spherical inclusions II. Ellipsoidal inclusions. *Journal of the Acoustical Society of America*, 68(6), 1820–1831. <https://doi.org/10.1121/1.385172>
- Bibring, J.-P., Langevin, Y., Gendrin, A., Gondet, B., Poulet, F., Berthé, M., et al. (2005). Mars surface diversity as revealed by the OMEGA/Mars Express observations. *Science*, 307(5715), 1576–1581. <https://doi.org/10.1126/science.1108806>
- Black, B. A., Manga, M., Ojha, L., Longpré, M.-A., Karunatilake, S., & Hlinka, L. (2022). The history of water in Martian magmas from thorium maps. *Geophysical Research Letters*, 49(11), e2022GL098061. <https://doi.org/10.1029/2022GL098061>
- Boynton, W., Ming, D., Kounaves, S., Young, S., Arvidson, R., Hecht, M., et al. (2009). Evidence for calcium carbonate at the Mars Phoenix landing site. *Science*, 325(5936), 61–64. <https://doi.org/10.1126/science.1172768>
- Brogli, C., & Ellis, D. (1990). Effect of alteration, formation absorption, and standoff on the response of the thermal neutron porosity log in gabbros and basalts: Examples from Deep Sea Drilling Project-Ocean Drilling Program Sites. *Journal of Geophysical Research*, 95(B6), 9171–9188. <https://doi.org/10.1029/JB095iB06p09171>
- Burr, D. M., Grier, J. A., McEwen, A. S., & Keszthelyi, L. P. (2002). Repeated aqueous flooding from the Cerberus Fossae: Evidence for very recently extant, deep groundwater on Mars. *Icarus*, 159(1), 53–73. <https://doi.org/10.1006/icar.2002.6921>
- Carr, M. (1987). Water on Mars. *Nature*, 326(6108), 30–35. <https://doi.org/10.1038/326030a0>
- Carr, M., & Head, J. (2002). Elevations of water-worn features on Mars: Implications for circulation of groundwater. *Journal of Geophysical Research*, 107(E12), 14–1. <https://doi.org/10.1029/2002JE001845>
- Carr, M., & Head, J. (2003). Oceans on Mars: An assessment of the observational evidence and possible fate. *Journal of Geophysical Research*, 108(E5), 5042. <https://doi.org/10.1029/2002JE001963>
- Carr, M., & Head, J. (2019). Mars: Formation and fate of a frozen Hesperian ocean. *Icarus*, 319, 433–443. <https://doi.org/10.1016/j.icarus.2018.08.021>
- Chen, J., Kuang, X., & Zheng, C. (2020). An empirical porosity–depth model for Earth’s crust. *Hydrogeology Journal*, 28(7), 2331–2339. <https://doi.org/10.1007/s10040-020-02214-x>
- Christensen, N. I. (1972). Compressional and shear wave velocities at pressures to 10 kilobars for basalts from the East Pacific Rise. *Geophysical Journal International*, 28(5), 425–429. <https://doi.org/10.1111/j.1365-246X.1972.tb06140.x>
- Citron, R. I., Manga, M., & Hemingway, D. J. (2018). Timing of oceans on Mars from shoreline deformation. *Nature*, 555(7698), 643–646. <https://doi.org/10.1038/nature26144>
- Clifford, S. M. (1993). A model for the hydrologic and climatic behavior of water on Mars. *Journal of Geophysical Research*, 98(E6), 10973–11016. <https://doi.org/10.1029/93JE00225>
- Clifford, S. M. (1997). The origin of the Martian intercrater plains: The role of liquefaction from impact and tectonic-induced seismicity. In *Lunar and Planetary Science Conference* (Vol. 28, p. 241). *Lunar and Planetary Science Conference*. Retrieved from <https://ui.adsabs.harvard.edu/abs/1997LPL...28..241C>

- Clifford, S. M. (1987). Mars: Crustal pore volume, cryospheric depth, and the global occurrence of groundwater. In V. Baker M. Carr, F. Fanale, R. Greeley, R. Haberle, C. Leovy, & T. Maxwell (Eds.), *MECA symposium on mars: Evolution of its climate and atmosphere* (p. 32). Retrieved from <https://ui.adsabs.harvard.edu/abs/1987meca.symp...32C>
- Clifford, S. M., Lasue, J., Heggy, E., Boisson, J., McGovern, P., & Max, M. D. (2010). Depth of the Martian cryosphere: Revised estimates and implications for the existence and detection of subpermafrost groundwater. *Journal of Geophysical Research*, *115*(E7), E07001. <https://doi.org/10.1029/2009JE003462>
- Clifford, S. M., & Parker, T. J. (2001). The evolution of the Martian hydrosphere: Implications for the fate of a primordial ocean and the current state of the northern plains. *Icarus*, *154*(1), 40–79. <https://doi.org/10.1006/icar.2001.6671>
- Colaprete, A., & Jakosky, B. M. (1998). Ice flow and rock glaciers on Mars. *Journal of Geophysical Research*, *103*(E3), 5897–5909. <https://doi.org/10.1029/97JE03371>
- Davies, J. H., & Davies, D. R. (2010). Earth's surface heat flux. *Solid Earth*, *1*(1), 5–24. <https://doi.org/10.5194/se-1-5-2010>
- Di Achille, G., & Hynek, B. M. (2010). Ancient ocean on Mars supported by global distribution of deltas and valleys. *Nature Geoscience*, *3*(7), 459–463. <https://doi.org/10.1038/ngeo891>
- Dou, S., Nakagawa, S., Dreger, D., & Ajo-Franklin, J. (2017). An effective-medium model for P-wave velocities of saturated, unconsolidated saline permafrost. *Geophysics*, *82*(3), EN33–EN50. <https://doi.org/10.1190/geo2016-0474.1>
- Dvorkin, J., & Nur, A. (1996). Elasticity of high-porosity sandstones: Theory for two North Sea data sets. *Geophysics*, *61*(5), 1363–1370. <https://doi.org/10.1190/1.1444059>
- Edwards, C., Nowicki, K., Christensen, P., Hill, J., Gorelick, N., & Murray, K. (2011). Mosaicking of global planetary image datasets: 1. Techniques and data processing for Thermal Emission Imaging System (THEMIS) multi-spectral data. *Journal of Geophysical Research*, *116*(E10), E10008. <https://doi.org/10.1029/2010JE003755>
- Franzson, H., Guðfinnsson, G., Helgadóttir, H., & Frolova, J. (2010). *Porosity, density and chemical composition relationships in altered Icelandic hyaloclastites*. CRC Press Inc.
- Golombek, M., Grott, M., Kargl, G., Andrade, J., Marshall, J., Warner, N., et al. (2018). Geology and physical properties investigations by the InSight lander. *Space Science Reviews*, *214*(5), 1–52. <https://doi.org/10.1007/s11214-018-0512-7>
- Goossens, S., Sabaka, T. J., Genova, A., Mazarico, E., Nicholas, J. B., & Neumann, G. A. (2017). Evidence for a low bulk crustal density for Mars from gravity and topography. *Geophysical Research Letters*, *44*(15), 7686–7694. <https://doi.org/10.1002/2017GL074172>
- Gyalay, S., Nimmo, F., Plesa, A.-C., & Wiczeorek, M. (2020). Constraints on thermal history of Mars from depth of pore closure below InSight. *Geophysical Research Letters*, *47*(16), e2020GL088653. <https://doi.org/10.1029/2020gl088653>
- Halevy, I., & Schrag, D. (2009). Sulfur dioxide inhibits calcium carbonate precipitation: Implications for early Mars and Earth. *Geophysical Research Letters*, *36*(23), L23201. <https://doi.org/10.1029/2009GL040792>
- Heap, M. J. (2019). P- and S-wave velocity of dry, water-saturated, and frozen basalt: Implications for the interpretation of Martian seismic data. *Icarus*, *330*, 11–15. <https://doi.org/10.1016/j.icarus.2019.04.020>
- Heap, M. J., Baumann, T. S., Rosas-Carbajal, M., Komorowski, J.-C., Gilg, H. A., Villeneuve, M., et al. (2021). Alteration-induced volcano instability at La Soufrière de Guadeloupe (Eastern Caribbean). *Journal of Geophysical Research: Solid Earth*, *126*(8), e2021JB022514. <https://doi.org/10.1029/2021JB022514>
- Heap, M. J., & Violay, M. E. (2021). The mechanical behaviour and failure modes of volcanic rocks: A review. *Bulletin of Volcanology*, *83*(5), 1–47. <https://doi.org/10.1007/s00445-021-01447-2>
- Hobiger, M., Hallo, M., Schmelzbach, C., Stähler, S., Fäh, D., Giardini, D., et al. (2021). The shallow structure of Mars at the InSight landing site from inversion of ambient vibrations. *Nature Communications*, *12*(1), 1–13. <https://doi.org/10.1038/s41467-021-26957-7>
- Jakosky, B. M. (2021). Atmospheric loss to space and the history of water on Mars. *Annual Review of Earth and Planetary Sciences*, *49*(1), 71–93. <https://doi.org/10.1146/annurev-earth-062420-052845>
- Jenkins, J., Johnson, D., La Ragione, L., & Makse, H. (2005). Fluctuations and the effective moduli of an isotropic, random aggregate of identical, frictionless spheres. *Journal of the Mechanics and Physics of Solids*, *53*(1), 197–225. <https://doi.org/10.1016/j.jmps.2004.06.002>
- Kilburn, R., Dasent, J., Wright, V., & Manga, M. (2022). *Lithology, pore-filling media, and pore closure depth beneath InSight on Mars inferred from shear wave velocities*. Zenodo. <https://doi.org/10.5281/zenodo.7301787>
- Kim, D., Banerdt, W., Ceylan, S., Giardini, D., Lekić, V., Lognonné, P., et al. (2022). Surface waves and crustal structure on Mars. *Science*, *378*(6618), 417–421. <https://doi.org/10.1126/science.abq7157>
- Knapmeyer-Endrun, B., Panning, M. P., Bissig, F., Joshi, R., Khan, A., Kim, D., et al. (2021). Thickness and structure of the Martian crust from InSight seismic data. *Science*, *373*(6553), 438–443. <https://doi.org/10.1126/science.abf8966>
- Lewis, K. W., Peters, S., Gonter, K., Morrison, S., Schmerr, N., Vasavada, A. R., & Gabriel, T. (2019). A surface gravity traverse on Mars indicates low bedrock density at Gale crater. *Science*, *363*(6426), 535–537. <https://doi.org/10.1126/science.abf8966>
- Li, J., Beghein, C., Wookey, J., Davis, P., Lognonné, P., Schimmel, M., et al. (2022). Evidence for crustal seismic anisotropy at the InSight lander site. *Earth and Planetary Science Letters*, *593*, 117654. <https://doi.org/10.1016/j.epsl.2022.117654>
- Lognonné, P., Banerdt, W., Pike, W., Giardini, D., Christensen, U., Garcia, R. F., et al. (2020). Constraints on the shallow elastic and anelastic structure of Mars from InSight seismic data. *Nature Geoscience*, *13*(3), 213–220. <https://doi.org/10.1038/s41561-020-0536-y>
- Lognonné, P., Banerdt, W. B., Giardini, D., Pike, W. T., Christensen, U., Laudet, P., et al. (2019). SEIS: InSight's seismic experiment for internal structure of Mars. *Space Science Reviews*, *215*(1), 1–170. <https://doi.org/10.1007/s11214-018-0574-6>
- Manga, M. (2004). Martian floods at Cerberus Fossae can be produced by groundwater discharge. *Geophysical Research Letters*, *31*(2), L02702. <https://doi.org/10.1029/2003GL018958>
- Manga, M., & Wright, V. (2021). No cryosphere-confined aquifer below InSight on Mars. *Geophysical Research Letters*, *48*(8), e2021GL093127. <https://doi.org/10.1029/2021GL093127>
- Manning, C., & Ingebritsen, S. (1999). Permeability of the continental crust: Implications of geothermal data and metamorphic systems. *Reviews of Geophysics*, *37*(1), 127–150. <https://doi.org/10.1029/1998RG900002>
- Mavko, G., Mukerji, T., & Dvorkin, J. (2020). *The rock physics handbook*. Cambridge University Press. <https://doi.org/10.1017/9781108333016>
- McSween, H. Y. (2015). Petrology on Mars. *American Mineralogist*, *100*(11–12), 2380–2395. <https://doi.org/10.2138/am-2015-5257>
- Mindlin, R. D. (1949). Compliance of elastic bodies in contact. *Journal of Applied Mechanics*, *16*(3), 259–268. <https://doi.org/10.1115/1.4009973>
- Ming, D., Niles, P., Morris, R., Boynton, W., Golden, D., Lauer, H., & Sutter, B. (2009). Thermal and evolved gas behavior of calcite under Mars Phoenix TEGA operating conditions. In *40th Lunar and Planetary Science Conference* (p. 1843). *Lunar and Planetary Science Conference*. Retrieved from <https://ui.adsabs.harvard.edu/abs/2009LPI....40.1843S>
- Mustard, J. F. (2019). Sequestration of volatiles in the Martian crust through hydrated minerals: A significant planetary reservoir of water. In *Volatiles in the Martian crust* (pp. 247–263). Elsevier. <https://doi.org/10.1016/B978-0-12-804191-8.00008-8>

- Nazari-Sharabian, M., Aghababaei, M., Karakouzian, M., & Karami, M. (2020). Water on Mars—A literature review. *Galaxies*, 8(2), 40. <https://doi.org/10.3390/galaxies8020040>
- Orosei, R., Lauro, S., Pettinelli, E., Cicchetti, A., Coradini, M., Cosciotti, B., et al. (2018). Radar evidence of subglacial liquid water on Mars. *Science*, 361(6401), 490–493. <https://doi.org/10.1126/science.aar7268>
- Pan, L., Quantin-Nataf, C., Tauzin, B., Michaut, C., Golombek, M., Lognonné, P., et al. (2020). Crust stratigraphy and heterogeneities of the first kilometers at the dichotomy boundary in western Elysium Planitia and implications for InSight lander. *Icarus*, 338, 113511. <https://doi.org/10.1016/j.icarus.2019.113511>
- Parro, L. M., Jiménez-Díaz, A., Mansilla, F., & Ruiz, J. (2017). Present-day heat flow model of Mars. *Scientific Reports*, 7(1), 1–9. <https://doi.org/10.1038/srep45629>
- Payré, V., Salvatore, M., & Edwards, C. (2019). An evolved early crust exposed on Mars revealed through spectroscopy. *Geophysical Research Letters*, 49(21), e2022GL099639. <https://doi.org/10.1029/2022GL099639>
- Rodríguez, J. A. P., Kargel, J. S., Baker, V. R., Gulick, V. C., Berman, D. C., Fairén, A. G., et al. (2015). Martian outflow channels: How did their source aquifers form and why did they drain so rapidly? *Scientific Reports*, 5(1), 1–10. <https://doi.org/10.1029/2003GL018958>
- Scheller, E., Ehlmann, B., Hu, R., Adams, D., & Yung, Y. (2021). Long-term drying of Mars by sequestration of ocean-scale volumes of water in the crust. *Science*, 372(6537), 56–62. <https://doi.org/10.1126/science.abc7717>
- Smrekar, S. E., Lognonné, P., Spohn, T., Banerdt, W. B., Breuer, D., Christensen, U., et al. (2019). Pre-mission InSights on the interior of Mars. *Space Science Reviews*, 215(1), 1–72. <https://doi.org/10.1007/s11214-018-0563-9>
- Tanaka, K. L., Skinner, J. A., Dohm, J. M., Irwin, R. P., III, Kolb, E. J., Fortezzo, C. M., et al. (2014). Geologic map of Mars (Report No. 3292). <https://doi.org/10.3133/sim3292>
- Te Wu, T. (1966). The effect of inclusion shape on the elastic moduli of a two-phase material. *International Journal of Solids and Structures*, 2(1), 1–8. [https://doi.org/10.1016/0020-7683\(66\)90002-3](https://doi.org/10.1016/0020-7683(66)90002-3)
- Toksöz, M. N., Cheng, C., & Timur, A. (1976). Velocities of seismic waves in porous rocks. *Geophysics*, 41(4), 621–645. <https://doi.org/10.1190/1.1440639>
- Tsuji, T., & Iturrino, G. J. (2008). Velocity-porosity relationships in oceanic basalt from eastern flank of the Juan de Fuca Ridge: The effect of crack closure on seismic velocity. *Exploration Geophysics*, 39(1), 41–51. <https://doi.org/10.1071/EG08001>
- Vanorio, T., Prasad, M., & Nur, A. (2003). Elastic properties of dry clay mineral aggregates, suspensions and sandstones. *Geophysical Journal International*, 155(1), 319–326. <https://doi.org/10.1046/j.1365-246X.2003.02046.x>
- Voigt, J. R., & Hamilton, C. W. (2018). Investigating the volcanic versus aqueous origin of the surficial deposits in Eastern Elysium Planitia, Mars. *Icarus*, 309, 389–410. <https://doi.org/10.1016/j.icarus.2018.03.009>
- Waite, W. F., Santamarina, J. C., Cortes, D. D., Dugan, B., Espinoza, D., Germaine, J., et al. (2009). Physical properties of hydrate-bearing sediments. *Reviews of Geophysics*, 47(4), RG4003. <https://doi.org/10.1029/2008RG000279>
- Wang, C.-Y., Manga, M., & Wong, A. (2005). Floods on Mars released from groundwater by impact. *Icarus*, 175(2), 551–555. <https://doi.org/10.1016/j.icarus.2004.12.003>
- Warner, N., Golombek, M., Ansan, V., Marteau, E., Williams, N., Grant, J., et al. (2022). In situ and orbital stratigraphic characterization of the InSight landing site—A type example of a regolith-covered lava plain on Mars. *Journal of Geophysical Research: Planets*, 127(4), e2022JE007232. <https://doi.org/10.1029/2022JE007232>
- Weiss, D. K., & Head, J. W. (2017). Evidence for stabilization of the ice-cemented cryosphere in earlier Martian history: Implications for the current abundance of groundwater at depth on Mars. *Icarus*, 288, 120–147. <https://doi.org/10.1016/j.icarus.2017.01.018>
- Wernicke, L. J., & Jakosky, B. M. (2021). Martian hydrated minerals: A significant water sink. *Journal of Geophysical Research: Planets*, 126(3), e2019JE006351. <https://doi.org/10.1029/2019JE006351>
- Wieczorek, M. A., Broquet, A., McLennan, S. M., Rivoldini, A., Golombek, M., Antonangeli, D., et al. (2022). InSight constraints on the global character of the Martian crust. *Journal of Geophysical Research: Planets*, 127(5), e2022JE007298. <https://doi.org/10.1029/2022JE007298>
- Woerber, A., Katz, S., & Ahrens, T. (1963). Elasticity of selected rocks and minerals. *Geophysics*, 28(4), 658–663. <https://doi.org/10.1190/1.1439242>
- Wright, V., Dasent, J., Kilburn, R., & Manga, M. (2022). A minimally cemented shallow crust beneath InSight. *Geophysical Research Letters*, 49(15), e2022GL099250. <https://doi.org/10.1029/2022GL099250>
- Zong, J., Stewart, R. R., Dyaur, N., & Myers, M. T. (2017). Elastic properties of rock salt: Laboratory measurements and Gulf of Mexico well-log analysis. *Geophysics*, 82(5), D303–D317. <https://doi.org/10.1190/geo2016-0527.1>